Photo-thermal synergistically catalytic conversion of glycerol and carbon dioxide to glycerol carbonate over Au/ZnWO$_4$-ZnO catalysts

Jiaxiong Liu[a], Yajin Li[a], Huimin Liu[a,b,*], Dehua He[a,*]

[a] Innovative Catalysis Program, Key Laboratory of Organic Optoelectronics and Molecular Engineering of Ministry of Education, Department of Chemistry, Tsinghua University, Beijing 100084, China
[b] School of Chemical and Biomolecular Engineering, The University of Sydney, NSW 2006, Australia

A B S T R A C T

Converting glycerol and CO$_2$ into glycerol carbonate offers a green pathway for utilizing biodiesel by-product glycerol and greenhouse gas CO$_2$ as well as synthesizing the important chemical compound glycerol carbonate. In this study, for the first time, the abundant visible light was introduced into thermal-driven glycerol carbonylation system, aiming to improve catalyst performance via breaking the thermodynamic equilibrium limitations. Here x%Au/ZnWO$_4$-ZnO catalysts were designed for the photo-thermal catalytic system. It was found that, ZnWO$_4$-ZnO itself was effective in glycerol carbonylation even under thermal-driven condition, and the loading of plasmonic Au further enhanced the catalytic performances especially with visible light irradiation. The visible light responsivity of the catalysts and reaction temperatures played important roles for the photo-thermal performance of x%Au/ZnWO$_4$-ZnO, indicating the strong photo-thermal synergistic effect for the highly promoted catalytic performance. This study suggests the photo-thermal synergistic catalysis is one of efficient approaches for further improving catalytic performance.

1. Introduction

Glycerol carbonate is an important compound in the chemical field as inert solvent, electrolyte of lithium ion batteries, and monomer of polycarbonate resins [1–4]. It ccould be synthesized via the direct reaction of glycerol, the major by-product of the biodiesel production process, with various sources of carbonyl functionality [5–7]. The use of renewable carbon source to produce glycerol carbonate is meaningful for sustainable development. Greenhouse gas CO$_2$ is a cheap, abundant and renewable carbon source [8–15]. Synthesizing glycerol carbonate from glycerol and CO$_2$ could comprehensively utilize biodiesel by-product and greenhouse gas, depicting a green and sustainable reaction pathway [1,10,16]. Heat could act as the driving force for the synthesis of glycerol carbonate from glycerol and CO$_2$, however, due to thermodynamic equilibrium limitations, the yield for target product glycerol carbonate is low, even in the presence of proper catalyst and under ultra-high reaction pressure (> 10.0 MPa) [1,10,16].

Photocatalysis is a research hotspot in recent years [9,17–22]. Introducing light into a thermal-driven catalytic reaction system could improve the performance of a proper catalyst [15,23–25]. Kong et al. reported that, the interleaved energy bands between semiconductors and the doping of plasmonic metal over Cu/NiO-MoO$_3$/SiO$_2$ and Cu/NiO-V$_2$O$_5$/SiO$_2$ photocatalysts benefited the effective separation of photo-generated electron-hole pairs, thereby promoted the activations of CO$_2$ and methanol and significantly enhanced the generation of product dimethyl carbonate under ultraviolet irradiation [26,27].

To date, there have been no literatures studying light assisted thermal-driven glycerol carbonylation by CO$_2$ to glycerol carbonate. Tailoring efficient catalysts and investigating light effects for this catalytic system would be of great significance both for fundamentally unravelling the reaction mechanism and practically providing a sustainable pathway for glycerol carbonate production. TiO$_2$, WO$_3$, CeO$_2$, Mo$_2$O$_3$, Bi$_2$S$_3$, Mo$_2$C, SiC, C$_3$N$_4$, ZnWO$_4$ and ZnO are classic semiconductors, and have been reported to be capable for photocatalytic CO$_2$ activation and reduction [28,29]. In this study, the photo-thermal catalytic performance of a series of single or composite semiconductors (the synthesis approaches are listed in Table S1) in the reaction of glycerol carbonate generation from glycerol and CO$_2$ were explored and screened (Table S2), with the results revealing that ZnWO$_4$-ZnO composite exhibited the highest photo-thermal catalytic performance among all the tested samples whereas there is still room for further improvement (Table S2). The ratio of ZnWO$_4$ to ZnO as well as the

---

calcination temperature was optimized (Table S3). Plasmonic metal nanoparticle (Au, Ag, Cu) decoration could efficiently enhance visible light absorption and drive reaction occurrence due to their localized surface plasmon resonance (LSPR) effects [30]. Herein, several different plasmonic metals (Au, Ag, Cu) decorated $ZnWO_4$-ZnO were synthesized and pre-screen test suggested that Au/$ZnWO_4$-ZnO exhibited higher glycerol carbonylation performance under visible light irradiation (Table S4) probably due to the stronger LSPR effect of Au. Therefore, this study focused on the photo-thermal synergistic catalysis of the typical x%Au/$ZnWO_4$-ZnO catalysts (x% represented the mass percentage of Au in the catalyst) in the reaction of glycerol and CO_2, and correlated their physicochemical properties with catalytic performances to uncover the photo-thermal synergistic effects in promoting the formation of glycerol carbonate.

2. Experimental

2.1. Catalyst preparation

ZnO was prepared by hydrothermal method. In a typical procedure, 3.56 g of $Zn(NO_3)_2 \cdot 6H_2O$ was dissolved in 40 mL deionized water to obtain the salt solution and 6.36 g of Na_2CO_3 was dissolved in 20 mL of deionized water to obtain the precipitation solution. Then the salt solution was added dropwisely to the precipitant solution under vigorous stir to form a milky white suspension. After stirring for another 20 min at room temperature, the white suspension was transferred to a hydrothermal autoclave and hydrothermally reacted at 120 °C for 24 h. The precipitate was washed by deionized water for 4 times, dried at 110 °C overnight, and calcined at 400 °C for 3 h to obtain ZnO.

$ZnWO_4$-ZnO (contained 10 wt% WO_3) was prepared using a simple impregnation method. 2.0 g ZnO support was added into 60 mL aqueous solution of ammonium metatungstate. After stirring for 12 h at room temperature, excessive water was removed by rotary evaporation. The obtained solid powder was dried in an oven at 110 °C for 12 h and then calcined at 400 °C for 3 h. The obtained sample was denoted as $ZnWO_4$-ZnO.

Au/$ZnWO_4$-ZnO was also prepared by impregnation method, similar with that of $ZnWO_4$-ZnO, except that $ZnWO_4$-ZnO and chloroauric acid were used as the support and Au precursor, respectively. The catalysts were dried at 110 °C for 12 h and calcined at 600 °C for 3 h, and marked as x%Au/$ZnWO_4$-ZnO, where x% represented the mass percentage of Au in the catalyst.

Preparation methods of other single and composite semiconductors are listed in Table S1.

2.2. Catalyst characterization

The crystalline structures of the x%Au/$ZnWO_4$-ZnO catalysts were characterized via X-ray diffraction (XRD) on a Rigaku X-Ray Diffractometer equipped with Ni filter and Cu Kα radiation ($\lambda = 1.5406$ Å, 40 kV, 200 mA). The average crystallite sizes (d) of metal particle and support were calculated by the line broadening method using Scherrer equation, $d = K\lambda/\beta\cos\theta$, where λ is the wavelength of X-ray, K is Scherrer constant taken as 0.89, β is determined as the width of the peak at half maximum height, and θ is the diffraction angle.

N_2 adsorption-desorption isotherms of the catalysts were determined using a Micromeritics TriStar II 3020 M-type absorber. The specific surface area of the sample was fitted using the Brunaurer–Emmett–Teller (BET) method, and the pore volume and pore size distribution were calculated by the Barrett–Joyner–Halenda (BJH) method (based on the desorption branch).

The light absorption capacities of the catalysts were characterized on the Hitachi U-3010 UV–vis spectrophotometer in the wavelength range of 200–800 nm, with $BaSO_4$ as a reference.

The local structure of the catalysts was characterized via Raman

spectroscopy on HORIBA Jobin Yvon LabRAM HR with a laser source wavelength of 514 nm and a scanning range of 100–1100 cm^{-1}.

The surface composition of the catalyst and the chemical state of the element were analyzed by X-ray photoelectron spectroscopy (XPS), and an energy spectrometer of the PHI Quantera SXM model of ULVAC-PHI was used. The binding energy of each element was calibrated by C1s (284.8 eV).

Photo-generated electron-hole transfer and recombination of Au-based photocatalysts were analyzed by steady-state fluorescence spectroscopy (PL) on Edinburgh FS5 fluorescence spectrometer.

The basic properties of the catalysts were determined by CO_2-temperature programmed desorption (CO_2-TPD) methods on CHEMBET 3000 TPR/TPD. In a typical experimental procedure, approximately 0.1 g sample was placed in a U-shaped quartz tube and pretreated in He gas (30 mL/min) at 400 °C for 30 min. After cooling down to 100 °C, the gas was switched to high purity CO_2 for adsorption for 30 min. Then He gas was purged for 30 min at the same temperature. Finally, it was raised to 800 °C at a rate of 15 °C/min under a He gas flow (30 mL/min). The desorption signal ($m/z = 44$ for CO_2) was detected by a quadrupole mass spectrometer DM200 m.

2.3. Catalyst evaluation

The reaction of glycerol carbonate production from glycerol and CO_2 was carried out in a stainless steel high pressure photoreactor (Yanzheng YZPR-100) with a built-in thermocouple, equipped with a set of heating and magnetic stirring systems. A high-pressure resistant quartz window was used for visible light introduction. A certain amount of glycerol, catalyst, solvent and CO_2 were added/charged into the autoclave. After reacting for a certain period of time, the liquid in the autoclave was quantitatively analyzed by gas chromatography using a Lunan-SP 6890 gas chromatograph equipped with an FID detector and a column of PEG 20M (30 m × 0.32 mm × 0.5 μm).

3. Results and discussion

3.1. Physicochemical properties of the support and Au-based catalysts

The crystalline structure of $ZnWO_4$-ZnO demonstrated that it was comprised of hexagonal phase ZnO (PDF card 36-1451) and monoclinic phase $ZnWO_4$ (PDF card 15-0774) (Fig. 1). Diffraction peaks attributed to cubic phase Au (PDF card 04-0784) appeared over the x%Au/$ZnWO_4$-ZnO (x% = 1%–4%) catalysts, suggesting Au nanoparticles
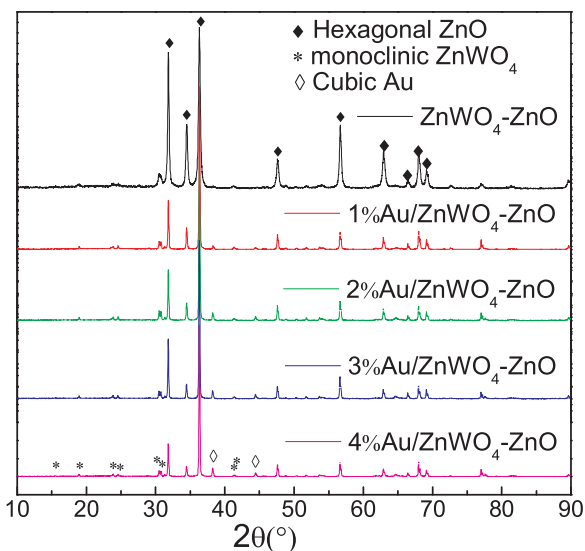

Fig. 1. XRD patterns of support $ZnWO_4$-ZnO and x%Au/$ZnWO_4$-ZnO catalysts.
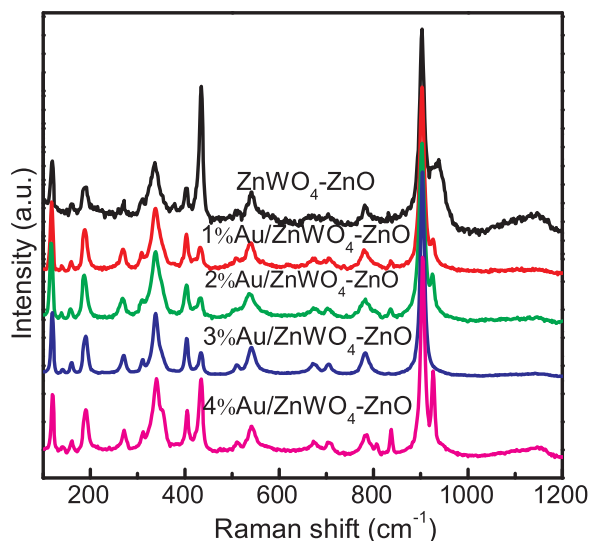
Fig. 2. Raman spectra of support $ZnWO_4$-ZnO and x%Au/$ZnWO_4$-ZnO catalysts.

Fig. 3. H_2-TPR profiles of support $ZnWO_4$-ZnO and x%Au/$ZnWO_4$-ZnO catalysts.

were loaded onto the support successfully. The sizes of ZnO and Au nanoparticles over $ZnWO_4$-ZnO and x%Au/$ZnWO_4$-ZnO catalysts were calculated according to Scherrer equation from the diffraction peaks at 36.3° (ZnO(101)) and 2θ = 38.2° (Au (111)). The sizes of ZnO were 34.8 nm, 66.8 nm, 65.2 nm, 65.4 nm, and 65.8 nm, respectively, and the sizes of Au nanoparticles were –, 55.0 nm, 64.9 nm, 69.2 nm, and 69.2 nm, respectively, over $ZnWO_4$-ZnO, 1%Au/$ZnWO_4$-ZnO, 2%Au/$ZnWO_4$-ZnO, 3%Au/$ZnWO_4$-ZnO and 4%Au/$ZnWO_4$-ZnO. It indicated that Au loading did not change the nanostructure of the $ZnWO_4$-ZnO support, but increased the sizes of ZnO nanoparticles, which was probably due to the aggregation of ZnO at the high temperatures used for catalyst drying and calcination during Au loading. Additionally, larger Au sizes were observed as the Au loading increased in the range of 1% to 3%.

The local structure of x%Au/$ZnWO_4$-ZnO catalysts was characterized by Raman spectroscopy. The results in Fig. 2 revealed that the Raman spectra of the x%Au/$ZnWO_4$-ZnO catalysts were similar to that of support $ZnWO_4$-ZnO, because of the relatively low Au loadings (≤ 4%). The peaks at 118 cm^{-1} and 434 cm^{-1} in Fig. 2 correspond to the characteristic E2 (low) and E2 (high) vibration modes of Wurtzite-structured ZnO, respectively [10]. The highest peak at 902 cm^{-1}, derived from the stretching vibration of the W−O bond anti-symmetric bridging mode in the tungstate chain, is typical for $ZnWO_4$; the peak at 335 cm^{-1} can be attributed to the terminal WO_2 functional group [16]; and W−O bond of medium length is a characteristic of bridged W−O, with its stretching vibration peaks in the range of 700–1000 cm^{-1}. The shift of the position of a specific Raman peak could reflect the degree of structure order, with blue shift suggesting the structural unit is more regular and red shift indicating more distortion [16]. The position of the peak at 902 cm^{-1} of the x%Au/$ZnWO_4$-ZnO catalysts did not change substantially with the variation of Au loading, indicating that the structural order of the $ZnWO_4$ component in each sample was similar and the length of the W−O bond in the octahedral WO_6 structure was basically constant. Results of XRD patterns and Raman spectra indicated the successful preparation of $ZnWO_4$-ZnO and x%Au/$ZnWO_4$-ZnO catalysts.

The actual contents of Au, Zn, and W in the catalysts were analyzed by ICP, and they were 1.9%, 71.5%, and 6.9%, respectively, over 2%Au/$ZnWO_4$-ZnO, close to the theoretical content of each element (2.0%, 70.9%, and 7.8%, respectively). The x%Au/$ZnWO_4$-ZnO catalysts possessed N_2 adsorption-desorption isotherms of IV category with H3 type hysteresis loops [17] and wide pore size distributions (10–90 nm), indicating that mesopores dominated the pore structures of the catalysts (Fig. S1 and Table S5). The reduction behaviours and Au-
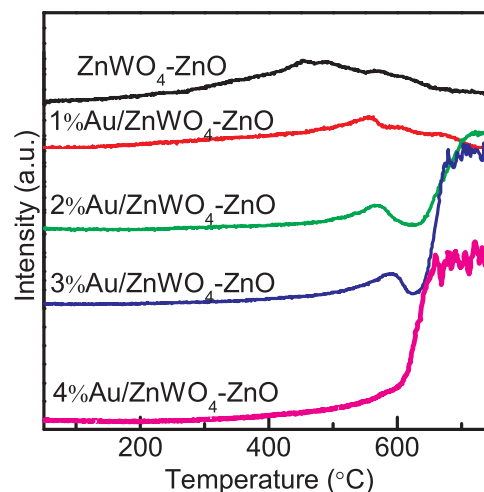
support interactions over the catalysts were investigated by H_2-TPR (Fig. 3). $ZnWO_4$-ZnO exhibited two partially overlapped peaks at 400–600 °C, which could respectively be assigned to the reduction of Zn^{2+} in small grains and large bulk particles to low valence species [23]. The two reduction peaks shifted to higher temperatures over x%Au/$ZnWO_4$-ZnO catalysts, suggesting that Au loading made Zn^{2+} more difficult to be reduced. The significantly changed reduction behaviour of the catalysts after Au loading provided evidences for the existence of strong interactions between Au nanoparticles and support $ZnWO_4$-ZnO.

3.2. XPS spectra of the support and Au-based catalysts

The chemical composition and oxidation state of surface of the x%Au/$ZnWO_4$-ZnO catalysts were characterized by XPS (Fig. 4 and Table 1). The full XPS spectra in Fig. 4a revealed Au, Zn, W and O were the main elements of x%Au/$ZnWO_4$-ZnO catalysts. The high resolution spectra of the three metal elements are displayed in Fig. 4b–d, respectively. Over $ZnWO_4$-ZnO, two peaks at 1022.1 eV and 1045.2 eV were observed over the Zn 2p spectra (Fig. 4c), corresponding to Zn 2p3/2 and Zn 2p1/2 [31], respectively; two partially overlapped peaks of W 4f appeared at 36.2 eV and 38.3 eV (Fig. 4d), corresponding to W 4f7/2 and W 4f5/2, respectively [31]. Over x%Au/$ZnWO_4$-ZnO catalysts, Au 4f 7/2 peak appeared at around 82.3 eV (Fig. 4b), close to that reported in the literatures [32,33]; the intensity of this peak increased gradually with the increase of Au loading, supporting the successful loading of Au; Zn and W could also be detected over x%Au/$ZnWO_4$-ZnO catalysts (evidenced by their typical XPS peaks in Fig. 4c and d), however, their peak positions shifted to lower binding energies, by 1.6 eV for Zn 2p and 1.5 eV for W 4f, respectively, which may be due to that the addition of Au increased the electron densities at the Zn and W points by partially transferring the electrons from the electronic rich Au to support $ZnWO_4$-ZnO [34]. However, as the Au content increased from 1% to 4%, the binding energies of Zn 2p and W 4f of x%Au/$ZnWO_4$-ZnO remained nearly constant, indicating that the loading content of Au had little effect on the electron density of Zn and W. The mass fractions of Au, W, Zn and O on surface of each catalyst calculated by XPS are shown in Table 1. As the theoretical loading of Au increased from 1% to 4%, the actual Au contents on the surface of the samples gradually increased from 0.5% to 2.8%, while the measured elemental contents of W and Zn on catalyst surface did not change much, indicating that Au could be impregnated onto $ZnWO_4$-ZnO and the impregnation of Au affected little on the support.

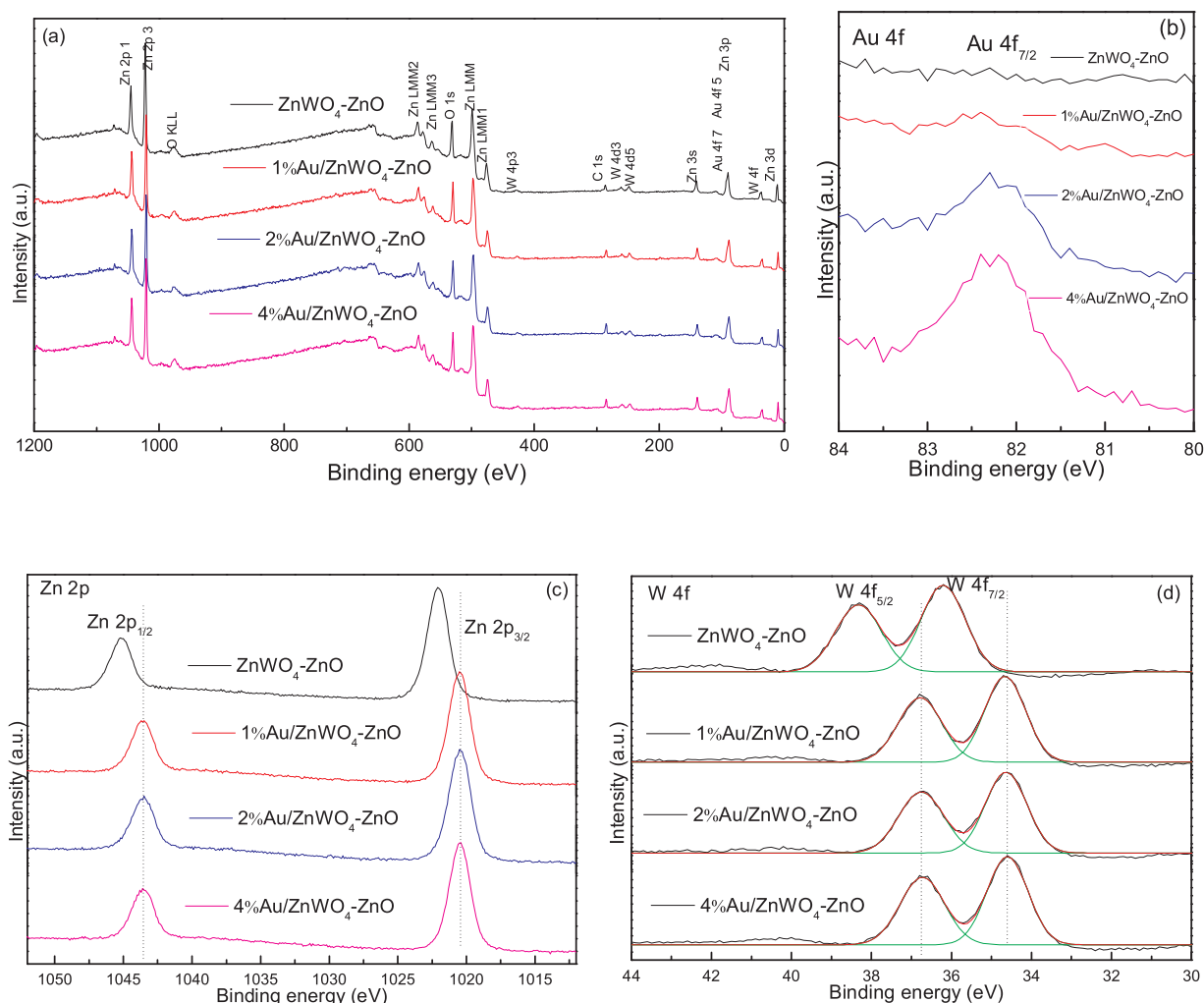**Fig. 4.** (a) Full XPS spectra, (b) Au 4f spectra, (c) Zn 2p spectra and (d) W 4f spectra of ZnWO$_4$-ZnO and x%Au/ZnWO$_4$-ZnO catalysts.

Table 1
Elemental contents over ZnWO$_4$-ZnO and x%Au/ZnWO$_4$-ZnO catalysts.

Catalyst	Mass fraction of each element (%)							
	Measured value				Theoretical value			
	Au	W	Zn	O	Au	W	Zn	O
ZnWO$_4$-ZnO	0	8.7	66.4	24.9	0	7.9	72.3	19.8
1%Au/ZnWO$_4$-ZnO	0.5	10.1	64.0	25.4	1.0	7.8	71.6	19.6
2%Au/ZnWO$_4$-ZnO	1.2	10.3	63.4	25.1	2.0	7.8	70.9	19.3
4%Au/ZnWO$_4$-ZnO	2.8	10.2	64.5	22.5	4.0	7.6	69.4	19.0

3.3. CO$_2$ adsorption-desorption capacities of the support and Au-based catalysts

Considering CO$_2$ is one of the reactants in the probe reaction, it is important to study the CO$_2$ adsorption-desorption properties of x%Au/ZnWO$_4$-ZnO. Herein, CO$_2$-TPD was performed with the results displayed in Fig. 5. Apparently, ZnWO$_4$-ZnO had a CO$_2$ desorption peak at the low temperature region (100–200 °C) and two concomitant CO$_2$ desorption peaks at the high temperature region (300–600 °C). The intensity of the desorption peaks reduced to some extents with the increase of Au loadings, probably due to the coverage of ZnWO$_4$-ZnO surface by Au nanoparticles. The areas of the CO$_2$ desorption peaks in the range of 100–200 °C, 200–400 °C, and > 400 °C were integrated (Table 2). Obviously, with the increase of Au loading from 0% to 4%,
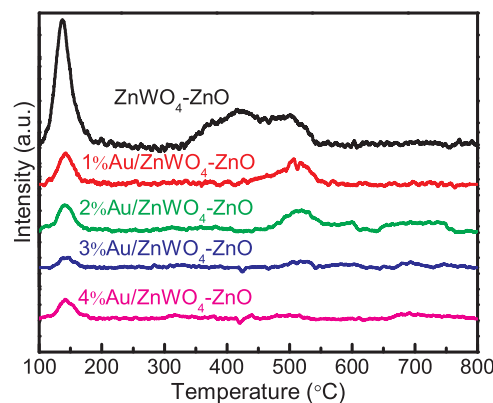

Fig. 5. CO$_2$-TPD profiles of ZnWO$_4$-ZnO and x%Au/ZnWO$_4$-ZnO catalysts.

the total basicity of the catalysts firstly dropped severely from 428.6 μmol CO$_2$/g (ZnWO$_4$-ZnO) to 93.0 μmol CO$_2$/g (1%Au/ZnWO$_4$-ZnO) and then decreased gradually and finally to 21.3 μmol CO$_2$/g (4%Au/ZnWO$_4$-ZnO).

3.4. Light responsive capacities of the support and Au-based catalysts

The light absorption capacities of the catalysts play determining roles in influencing their photocatalytic performances. The UV–vis

Table 2
Basic sites over ZnWO$_4$-ZnO and x%Au/ZnWO$_4$-ZnO catalysts.

Catalyst	Basic sites (μmol CO$_2$/g)			
	100–200 °C	200–400 °C	> 400 °C	Total
ZnWO$_4$-ZnO	169.65	106.04	152.88	428.58
1%Au/ZnWO$_4$-ZnO	30.64	1.39	60.92	92.95
2%Au/ZnWO$_4$-ZnO	15.49	2.91	40.93	59.32
$_4$-ZnO	11.16	0.00	11.87	23.03
4%Au/ZnWO$_4$-ZnO	15.22	4.33	1.76	21.31

spectra in Fig. 6a revealed that, x%Au/ZnWO$_4$-ZnO exhibited similar trend in light absorption in the wavelength range of 200–390 nm, indicating the amount of Au loading did not affect the optical responsivity of ZnWO$_4$-ZnO in the ultraviolet region. What's more, compared with ZnWO$_4$-ZnO, the light absorption intensities of x%Au/ZnWO$_4$-ZnO were lower in the wavelength range of 200–320 nm, which may be owing to the sintering of ZnWO$_4$-ZnO nanoparticles, whereas the light absorption capacities of the catalysts in the visible light region were greatly enhanced because of LSPR effect of the supported Au nanoparticles [7]. The strong visible light absorption ensures the x%Au/ZnWO$_4$-ZnO catalysts could be excited by visible light and produce photo-generated electron-hole pairs under visible light illumination. Noticeably, 3%Au/ZnWO$_4$-ZnO and 2%Au/ZnWO$_4$-ZnO performed stronger visible light absorption capacity than other catalysts, evidenced by their larger Au plasmonic absorption peaks in the visible light region.

Steady-state fluorescence spectroscopy (PL) was used to analyze the transfer and recombination characteristics of the electron-hole pairs, another factor influencing the photocatalytic performance of the catalysts. Literatures [24] pointed out that ZnO has two main emission peaks on its PL spectra, in which the emission peak at about 390 nm is attributed to the recombination of photo-generated electron-hole pair, and the other emission peak located at 420–620 nm may be related to an indirect emission from ZnO surface vacancies [24]. The strongest emission peak of ZnWO$_4$ appears at around 470 nm, which is derived from the WO$_6^{6-}$ structure of the scheelite-type ZnWO$_4$ [15]. The PL spectra in Fig. 6b revealed that, the intensity of the emission peak at around 390 nm over 2%Au/ZnWO$_4$-ZnO was much lower than that of ZnWO$_4$-ZnO which indicated that the addition of 2% Au could effectively inhibit the recombination of photo-generated electron-hole pair in ZnWO$_4$-ZnO [25].
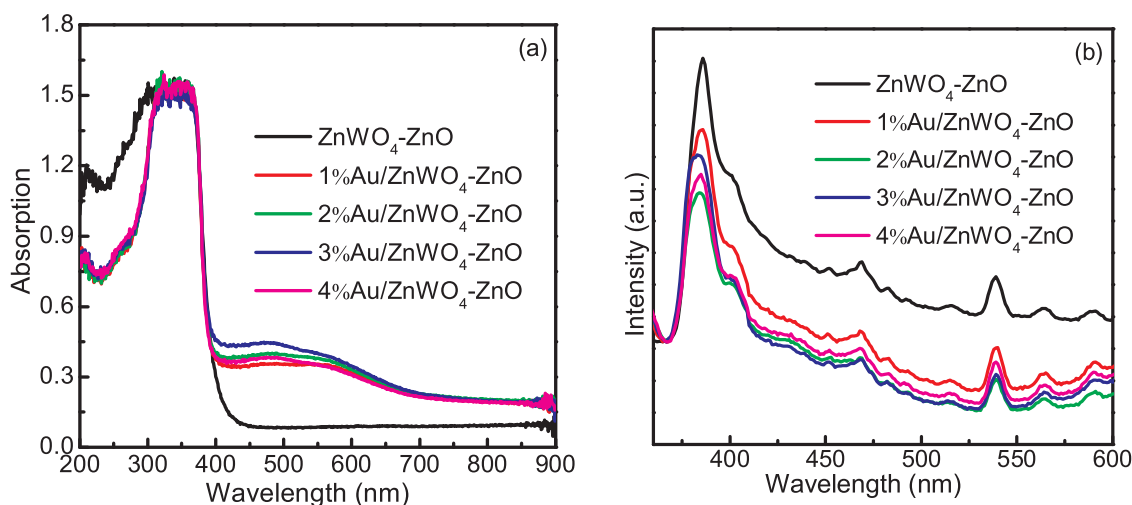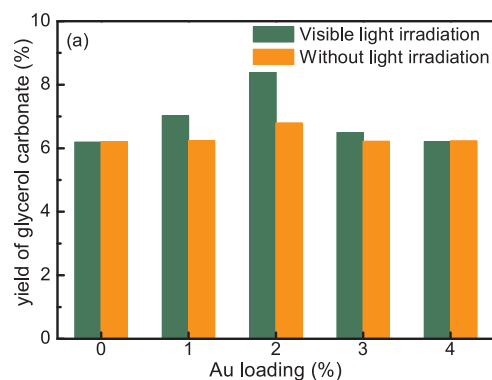

Fig. 7. Catalytic performance of x% Au/ZnWO$_4$-ZnO catalysts with or without visible light irradiation. L7.
Reaction conditions: 10 mmol glycerol, 1.0 g catalyst, 20 mL DMF, 5.0 MPa, 150 °C, 6 h, dark or with 250 W visible light irradiation.

3.5. Catalytic performances of the support and Au-based catalysts

The catalytic performances of ZnWO$_4$-ZnO and x%Au/ZnWO$_4$-ZnO catalysts were evaluated in the reaction of glycerol carbonate production from glycerol and CO$_2$ with or without visible light irradiation (Fig. 7). Under the conditions of 10 mmol glycerol, 1.0 g catalyst, 20 mL DMF, 150 °C, 5.0 MPa, 6 h, no matter with or without visible light irradiation, nearly 100% selectivity to glycerol carbonate could be achieved and by-products such as ether polymers were not detected. Without light irradiation, a yield of glycerol carbonate of 6.2% was obtained over ZnWO$_4$-ZnO, which increased slightly after the loading of Au (6.8% over 2%Au/ZnWO$_4$-ZnO), indicating Au helped reactant activation, however the promotion effect was very limited. With the irradiation of 250 W visible light, the photocatalytic performance of ZnWO$_4$-ZnO was almost the same as that obtained under the condition without light irradiation, which was due to the lack of visible light absorption capacity of ZnWO$_4$-ZnO; after the loading of Au, a volcano trend was observed over the increment of yield of glycerol carbonate, with a maximum yield increment of 1.6% being obtained when the loading of Au was 2%. It indicated that the amount of Au loading was important in improving the catalyst performance with visible light irradiation.

Reaction temperature is important in determining the photothermal catalytic activity of 2% Au/ZnWO$_4$-ZnO in glycerol carbonate synthesis (Fig. 8a). Without light irradiation, the conversion of glycerol increased gradually with increasing temperature from 110 °C to 150 °C,
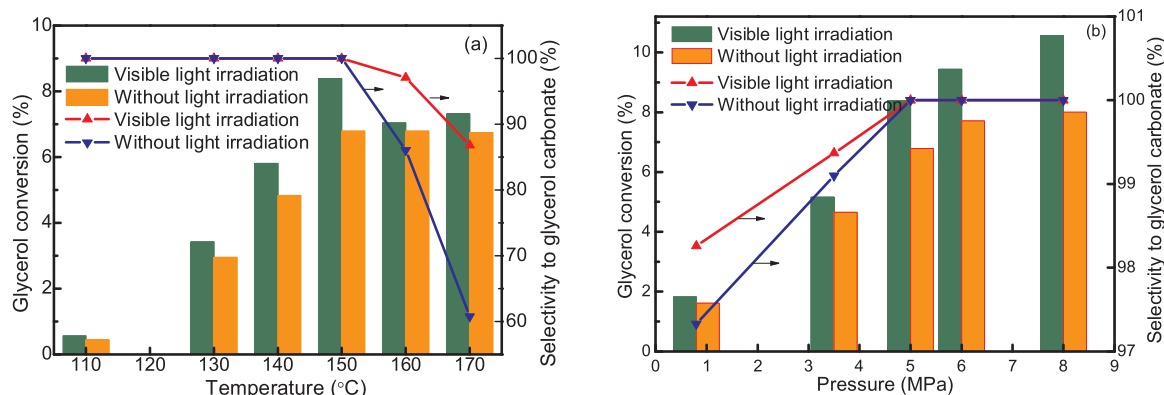

Fig. 6. (a) UV–vis spectra, and (b) PL spectra of ZnWO$_4$-ZnO and x%Au/ZnWO$_4$-ZnO catalysts.

Fig. 8. (a) effects of reaction temperatures on the performance of 2% Au/ZnWO$_4$-ZnO catalyst, and (b) Effects of pressure on the performance of 2% Au/ZnWO$_4$-ZnO catalyst.

Reaction conditions: 10 mmol glycerol, 1.0 g catalyst, 20 mL DMF, 6 h, dark or with 250 W visible light irradiation. The results in Fig. 8a was evaluated at 5.0 MPa, and the results in Fig. 8b was evaluated at 150 °C.

and then remained nearly constant when the temperature was further increased to 170 °C. In addition, the selectivity to glycerol carbonate decreased from 100% at 150 °C to 60.8% at 170 °C, due to the formation of by-product ether polymer at higher temperatures. On the other hand, the conversion of glycerol under visible light irradiation showed a volcanic curve with the increase of temperature, and reached the maximum value at 150 °C. Noticeably, by introducing 250 W visible light at 170 °C, the conversion of glycerol increased from 6.8% to 7.3%, and the selectivity to glycerol carbonate increased from 60.8% to 86.8%. The obviously improved glycerol conversion and selectivity to glycerol carbonate via visible light introduction at 150–170 °C, as well as the temperature-dependent photo-thermal performance of 2% Au/ZnWO$_4$-ZnO, suggested the existence of strong photo-thermal synergism over the photo-thermal catalytic system.

Reaction pressure also showed remarkable influence on the conversion and selectivity of carbonate, as shown in Fig. 8b. Fig. 8b shows the effect of CO$_2$ pressure on the photo-thermal catalytic activity of 2%Au/ZnWO$_4$-ZnO. With the increase of the reaction pressure from 0.8 MPa to 8.0 MPa, the conversion of glycerol increased gradually under the conditions of both with and without visible light irradiation, and the effect of light (the increment of glycerol conversion induced by visible light irradiation) was also increased gradually. When the reaction pressure is 8.0 MPa, the conversions of glycerol were 10.6% and 8%, respectively, under the conditions of with or without visible light radiation, suggesting an obvious photo-thermal catalytic effect. In addition, at lower CO$_2$ reaction pressure (0.8 to 3.5 MPa), a small amount of polyether polymer can be detected as by-products; at CO$_2$ reaction pressures of higher than 5.0 MPa, the selectivity to glycerol carbonate was close to 100%. Noteworthy, when CO$_2$ reaction pressure was low, the introduction of visible light could also slightly improve the selectivity to glycerol carbonate and reduce the formation of by-products.

3.6. Mechanism discussion

Based on the characterization and reaction results, a possible mechanism was proposed for the photo-thermal catalytic conversion of glycerol and CO$_2$ to glycerol carbonate. Without light irradiation, CO$_2$ and glycerol are activated on ZnWO$_4$-ZnO in the form of bridged carbonate and zinc alcohol complex, followed by the insertion of the activated CO$_2$ into the zinc alcohol complex to form a cyclic metal carbonate intermediate, and then the alkoxy in the intermediate nucleophilically attacks on carbon atom of carbonyl group, which finally rearranges to glycerol carbonate [4] The loading of Au reduced CO$_2$ adsorption-desorption capacities of ZnWO$_4$-ZnO (evidenced by the decreased CO$_2$ desorption peaks over the CO$_2$-TPD profile in Fig. 5) but facilitated CO$_2$ activation [26], with the two contradictory effects

leading to the nearly un-promoted catalytic performances of Au catalysts under the conditions without light irradiation. At the temperatures ≤ 150 °C, the above mentioned pathway dominated and lead to nearly 100% selectivity to glycerol carbonate. At temperatures > 150 °C, most of the adsorbed CO$_2$ molecules desorb from catalyst surface to free CO$_2$ (It could be seen from the CO$_2$-TPD profiles in Fig. 5); then the excessively adsorbed glycerol molecules tend to aggregate and form by-products ether polymers, and result in the decrease in selectivity to glycerol carbonate.

Under visible light irradiation, the hot electrons induced by Au LSPR could be excited and distributed over the energy states above Fermi energy level. Due to the combination between ZnO and ZnWO$_4$ as well as the Schottky barrier between metal Au and semiconductor, the photo-generated electron-hole pairs redistributed in the catalyst. The energy level of Au LSPR is higher than that of the conduction band of ZnO and ZnWO$_4$, which results in the transfer of the energetic conductive electrons of Au LSPR from the metal surface to the conduction band of ZnO and ZnWO$_4$. Then the electrons could be directly transferred to the antibonding orbitals of CO$_2$ molecules adsorbed on support ZnWO$_4$-ZnO, forming transient negative-ion state CO$_2$·$^-$ radicals [35–38] (CO$_2$·$^-$ was adsorbed on the support in this study, with its structure displayed in Fig. 9). The bonds in CO$_2$·$^-$ are weakened and CO$_2$ activation are then facilitated. Moreover, due to the electronegativity difference between C and O, O has more affinity to the electron and C is relatively positive charged. On the other hand, glycerol firstly chemically adsorbed on support by losing two H from the adjacent two hydroxyl groups (by reacting the two H atoms with O on the support) and then the positively charged hole preferably locates at the C atom and the adjacent O atom is relatively negatively charged since C has lower electronegativity than O. Due to the affinity between negatively and positively charged atoms, the O atom on the hydroxyl group of the activated alcohol attacks the C atom on the bridge coordinated carbonyl group and finally forms the target product glycerol carbonate by releasing one oxygen atom to compensate to support (Fig. 9). The possibility of glycerol carbonate formation via visible light irradiation is responsible for the enhanced photo-thermal activities over Au/ZnWO$_4$-ZnO. The transfer of photo-generated electrons and holes from catalysts to CO$_2$ and glycerol ensures stronger absorption of the reactants, which inhibits CO$_2$ desorption at higher temperatures and leads to the improved selectivity to glycerol carbonate.

4. Conclusions

To sum up, light is introduced into a thermal-driven catalytic system and for the first time used as driving force for the direct synthesis of glycerol carbonate from glycerol and CO$_2$. Visible light irradiation
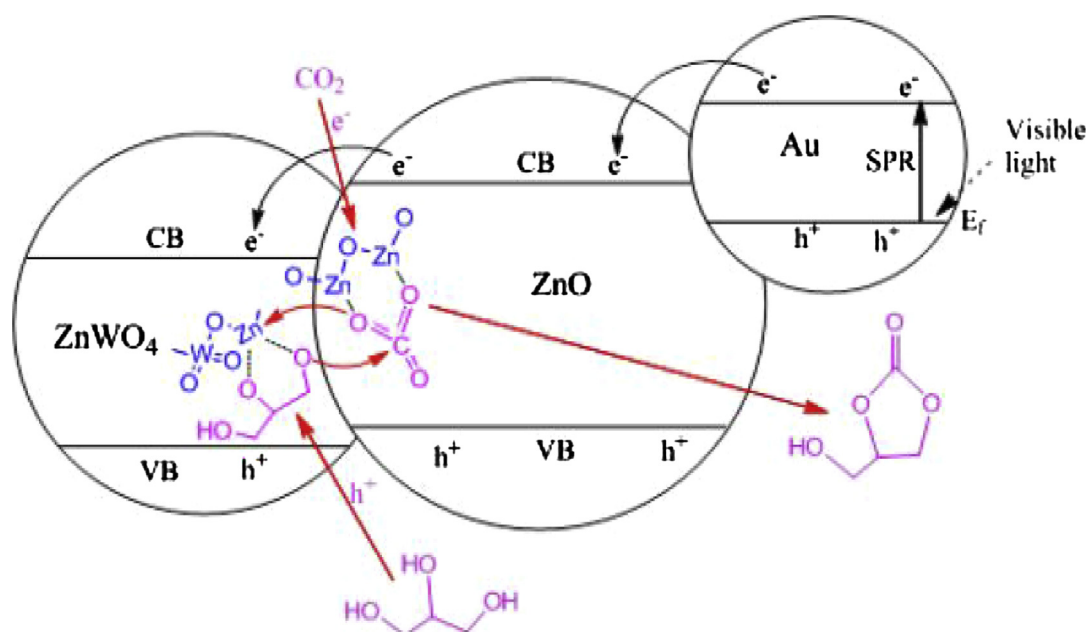
Fig. 9. Possible mechanism for catalytic conversion of glycerol and carbon dioxide to glycerol carbonate over Au/ZnWO$_4$-ZnO with light irradiation.

obviously improved the performances of x%Au/ZnWO$_4$-ZnO due to a strong photo-thermal synergistic effect. The light effects of the catalyst varied greatly with the contents of Au loading, with 2%Au/ZnWO$_4$-ZnO exhibiting the best photo-thermal catalytic performance. Under the condition of 150 °C, 8.0 MPa CO$_2$ and visible light irradiation, a yield to glycerol carbonate high up to 10.6% could be achieved, which was increased by 33% compared with the thermal-driven condition. The strong visible light absorption ability of the catalyst and the efficient separation of photo-generated electron-hole pairs are responsible for the excellent photocatalytic performances. This study offers an approach for effectively promoting catalytic performance via designing suitable catalysts with strong photo-thermal synergistic effect.

Acknowledgements

Appendix A. Supplementary data

Supplementary material related to this article can be found, in the online version, at doi:https://doi.org/10.1016/j.apcatb.2018.12.018.

References

[1] L.P. Ozorio, C.J.A. Mota, Direct carbonation of glycerol with CO$_2$ catalyzed by metal oxides, ChemPhysChem 18 (2017) 3260–3265.
[2] M.J. Climent, A. Corma, P. De Frutos, S. Iborra, M. Noy, A. Velty, P. Concepcion, Chemicals from biomass: synthesis of glycerol carbonate by transesterification and carbonylation with urea with hydrotalcite catalysts. The role of acid-base pairs, J. Catal. 269 (2010) 140–149.
[3] Z. Herseczki, T. Varga, G. Marton, Synthesis of glycerol carbonate from glycerol, a by-product of biodiesel production, Int. J. Chem. React. Eng. 7 (2009).
[4] T. Mizuno, T. Nakai, M. Mihara, New synthesis of glycerol carbonate from glycerol using sulfur-assisted carbonylation with carbon monoxide, Heteroatom Chem. 21 (2010) 99–102.
[5] Y.T. Algoufi, B.H. Hameed, Synthesis of glycerol carbonate by transesterification of glycerol with dimethyl carbonate over K-zeolite derived from coal fly ash, Fuel Process. Technol. 126 (2014) 5–11.
[6] Y.T. Algoufi, G. Kabir, B.H. Hameed, Synthesis of glycerol carbonate from biodiesel by-product glycerol over calcined dolomite, J. Taiwan Inst. Chem. E 70 (2017) 179–187.
[7] M. Aresta, A. Dibenedetto, F. Nocito, C. Pastore, A study on the carboxylation of glycerol to glycerol carbonate with carbon dioxide: the role of the catalyst, solvent and reaction conditions, J. Mol. Catal. A: Chem. 257 (2006) 149–153.
[8] M.P. Jiang, Z.D. Li, Y.Y. Yu, H.J. Wu, W. Li, D.Q. Ji, Y. Liu, Z.W. He, Z.H. Zhang, Efficient conversion of greenhouse gas of CO$_2$ into carbon products with desirable structures via molten carbonates electrolysis, J. Electrochem. Soc. 164 (2017) D1022–D1027.
[9] S.W. Liu, F. Chen, S.T. Li, X.X. Peng, Y. Xiong, Enhanced photocatalytic conversion of greenhouse gas CO$_2$ into solar fuels over g-C3N4 nanotubes with decorated transparent ZIF-8 nanoclusters, Appl. Catal. B: Environ. 211 (2017) 1–10.
[10] J.W. Ren, M. Johnson, R. Singhal, S. Licht, Transformation of the greenhouse gas CO$_2$ by molten electrolysis into a wide controlled selection of carbon nanotubes, J. CO$_2$ Util. 18 (2017) 335–344.
[11] Q. Zhang, M.Y. Mao, Y.Z. Li, Y. Yang, H. Huang, Z.K. Jiang, Q.Q. Hu, S.W. Wu, X.J. Zhao, Novel photoactivation promoted light-driven CO$_2$ reduction by CH4 on Ni/CeO2 nanocomposite with high light-to-fuel efficiency and enhanced stability, Appl. Catal. B: Environ. 239 (2018) 555–564.
[12] M.Y. Mao, Q. Zhang, Y. Yang, Y.Z. Li, H. Huang, Z.K. Jiang, Q.Q. Hu, X.J. Zhao, Solar-light-driven CO$_2$ reduction by methane on Pt nanocrystals partially embedded in mesoporous CeO2 nanorods with high light-to-fuel efficiency, Green Chem. 20 (2018) 2857–2869.
[13] H. Huang, M.Y. Mao, Q. Zhang, Y.Z. Li, J.L. Bai, Y. Yang, M. Zeng, X.J. Zhao, Solar-light-driven CO$_2$ reduction by CH4 on silica-cluster-modified Ni nanocrystals with a high solar-to-fuel efficiency and excellent durability, Adv. Energy Mater. 8 (2018) 1702472.
[14] H.M. Liu, X.G. Meng, T.D. Dao, H.B. Zhang, P. Li, K. Chang, T. Wang, M. Li, T. Nagao, J.H. Ye, Conversion of carbon dioxide by methane reforming under visible-light irradiation: surface-plasmon-mediated nonpolar molecule activation, Angew. Chem. Int. Ed. 54 (2015) 11545–11549.
[15] H.M. Liu, M. Li, T.D. Dao, Y.Y. Liu, W. Zhou, L.Q. Liu, X.G. Meng, T. Nagao, J.H. Ye, Design of PdAu alloy plasmonic nanoparticles for improved catalytic performance in CO$_2$ reduction with visible light irradiation, Nano Energy 26 (2016) 398–404.
[16] J.X. Liu, D.H. He, Transformation of CO$_2$ with glycerol to glycerol carbonate by a novel ZnWO4-ZnO catalyst, J. CO$_2$ Util. 26 (2018) 370–379.
[17] K. Wenderich, G. Mul, Methods, mechanism, and applications of photodeposition in photocatalysis: a review, Chem. Rev. 116 (2016) 14587–14619.
[18] M. Humayun, F. Raziq, A. Khan, W. Luo, Modification strategies of TiO2 for potential applications in photocatalysis: acritical review, Green Chem. Lett. Rev. 11 (2018) 86–102.
[19] M.Y. Mao, Y.Z. Li, J.T. Hou, M. Zeng, X.J. Zhao, Extremely efficient full solar spectrum light driven thermocatalytic activity for the oxidation of VOCs on OMS-2 nanorod catalyst, Appl. Catal. B: Environ. 174 (2015) 496–503.
[20] F. Liu, M. Zeng, Y.Z. Li, Y. Yang, M.Y. Mao, X.J. Zhao, UV–vis-infrared light driven thermocatalytic activity of octahedral layered birnessite nanoflowers enhanced by a novel photoactivation, Adv. Funct. Mater. 26 (2016) 4518–4526.
[21] Y. Yang, Y.Z. Li, Q. Zhang, M. Zeng, S.W. Wu, L. Lan, X.J. Zhao, Novel photo-activation and solar-light-driven thermocatalysis on epsilon-MnO2 nanosheets lead to highly efficient catalytic abatement of ethyl acetate without acetaldehyde as unfavorable by-product, J. Mater. Chem. A 6 (2018) 14195–14206.
[22] C.Y. Zhou, L. Cheng, Y.Z. Li, M. Zeng, Y. Yang, J.C. Wu, X.J. Zhao, Novel photo-activation promotes catalytic abatement of CO on CuO mesoporous nanosheets with full solar spectrum illumination, Appl. Catal. B: Environ. 225 (2018) 314–323.
[23] H.M. Liu, CO$_2$conversion through methane reforming under visible light: surface

plasmon mediated nonpolar molecule activation, Abstr. Pap. Am. Chem. Soc. 251 (2016).

[24] H.M. Liu, T.D. Dao, L.Q. Liu, X.G. Meng, T. Nagaoa, J.H. Ye, Light assisted CO_2 reduction with methane over group VIII metals: universality of metal localized surface plasmon resonance in reactant activation, Appl. Catal. B: Environ. 209 (2017) 183–189.

[25] H.M. Liu, X.G. Meng, T.D. Dao, L.Q. Liu, P. Li, G.X. Zhao, T. Nagao, L.Q. Yang, J.H. Ye, Light assisted CO_2 reduction with methane over SiO2 encapsulated Ni nanocatalysts for boosted activity and stability, J. Mater. Chem. A 5 (2017) 10567–10573.

[26] L.L. Kong, S.H. Zhong, Y. Liu, X.F. Xiao, Study on photo-catalytic synthesis of dimethyl carbonate from CO_2 and CH_3OH over Cu/NiO-V_2O_5/SiO_2 catalyst, Acta Chim. Sin. 64 (2006) 409–414.

[27] L.L. Kong, S.H. Zhong, Y. Liu, Photocatalytic reaction for synthesis of dimethyl carbonate from CO_2 and CH3OH over Cu/NiO-MoO_3/SiO_2 catalyst, Chin. J. Catal. 26 (2005) 917–922.

[28] J. Mao, K. Li, T.Y. Peng, Recent advances in the photocatalytic CO_2 reduction over semiconductors, Catal. Sci. Technol. 3 (2013) 2481–2498.

[29] S.N. Habisreutinger, L. Schmidt-Mende, J.K. Stolarczyk, Photocatalytic reduction of CO_2 on TiO_2 and other semiconductors, Angew. Chem. Int. Ed. 52 (2013) 7372–7408.

[30] X.J. Lang, X.D. Chen, J.C. Zhao, Heterogeneous visible light photocatalysis for selective organic transformations, Chem. Soc. Rev. 43 (2014) 473–486.

[31] Y. Keereeta, S. Thongtem, T. Thongtem, Enhanced photocatalytic degradation of methylene blue by WO_3/$ZnWO_4$ composites synthesized by a combination of microwave-solvothermal method and incipient wetness procedure, Powder Technol. 284 (2015) 85–94.

[32] A.M. Venezia, L.F. Liotta, G. Pantaleo, V. La Parola, G. Deganello, A. Beck, Z. Koppany, K. Frey, D. Horvath, L. Guczi, Activity of SiO_2 supported gold-palladium catalysts in CO oxidation, Appl. Catal. A: Gen. 251 (2003) 359–368.

[33] A. Zwijnenburg, A. Goossens, W.G. Sloof, M.W.J. Craje, A.M. van der Kraan, L.J. de Jongh, M. Makkee, J.A. Moulijn, XPS and Mossbauer characterization of Au/TiO_2 propene epoxidation catalysts, J. Phys. Chem. B 106 (2002) 9853–9862.

[34] N.S. Parmar, J.W. Choi, L.A. Boatner, M.D. McCluskey, K.G. Lynn, Formation of high concentrations of isolated Zn vacancies and evidence for their acceptor levels in ZnO, J. Alloys Compd. 729 (2017) 1031–1037.

[35] P. Christopher, H.L. Xin, S. Linic, Visible-light-enhanced catalytic oxidation reactions on plasmonic silver nanostructures, Nat. Chem. 3 (2011) 467–472.

[36] H. Song, X.G. Meng, T.D. Dao, W. Zhou, H.M. Liu, L. Shi, H.B. Zhang, T. Nagao, T. Kako, J.H. Ye, Light-enhanced carbon dioxide activation and conversion by effective plasmonic coupling effect of Pt and Au nanoparticles, ACS Appl. Mater. Interfaces 10 (2018) 408–416.

[37] R.G. Hobbs, W.P. Putnam, A. Fallahi, Y.J. Yang, F.X. Kartner, K.K. Berggren, Mapping photoemission and hot-electron emission from plasmonic nanoantennas, Nano Lett. 17 (2017) 6069–6076.

[38] M. Kim, M. Lin, J. Son, H.X. Xu, J.M. Nam, Hot-electron-mediated photochemical reactions: principles, recent advances, and challenges, Adv. Opt. Mater. 5 (2017) 21.